

15 The Angular Distribution of Light Emitted by Sonoluminescent Bubbles

A. Madrazo¹, M. Nieto-Vesperinas¹, and N. García²

¹ Instituto de Ciencia de Materiales de Madrid,
Consejo Superior de Investigaciones Científicas,
Cantoblanco, E-28049 Madrid, Spain.

² Laboratorio de Física de Sistemas Pequeños y Nanotecnología,
Consejo Superior de Investigaciones Científicas,
Serrano 144, E-28006 Madrid, Spain.

Abstract. Sonoluminescent bubbles constitute a new kind of microparticles, which *cavitate* (expand and collapse) due to sound action, with remarkable properties of light radiation. The observation of sonoluminescence in bubbles has opened an active research on a phenomenon of light radiation by sound conversion. Experiments have been performed on emission spectra, estimation of the bubble size by light scattering, assessment of the shape and its possible departure from dipole radiation angular correlations, and concerning the reactive nature of the gas inside the bubble. Several theories have been put forward, like e.g.: those that support the sphericity of the bubble; those that establish that it is actually non spherical, the emission being due to a jet implosion in which one half of the bubble collapses into the other half ; models to explain the dipole strength of a surrounding stream as experimentally observed ; and suggestions that the emission should rather originate in the liquid enclosing the bubble. However, the key problem of determining the size and shape of the bubble at the interval (50 ps) of emission has only recently been solved. Angular correlations from intensity measurements of the detected sonoluminescent flashes, diffracted by the bubble surface at the emission instant have been reported. We review here the theory on the angular distribution of the light emitted from several bubble shapes and sizes. This allows to establish which one matches with the experiments. For instance, it is found that an ellipsoidal shape of 1.5 to 2 μm and eccentricity 0.2 exhibits an excellent agreement with the existing data at all ranges of wavelengths.

1 Tutorial Background

1.1 Current Problems in Sonoluminescence

A bubble, produced in liquid, may radiate light under the action of a sound wave. The acoustic frequency usually is in the range 26 – 60 kHz and the intensity about 110 decibels. This conversion of sound into light is known as *sonoluminescence*. The phenomenon was first discovered in the 1930's as the shining from a water filled vessel with many air bubbles inside. However, recently, this effect has experienced a renewed and more detailed research [1–3], and now more controlled experiments have been conducted in which

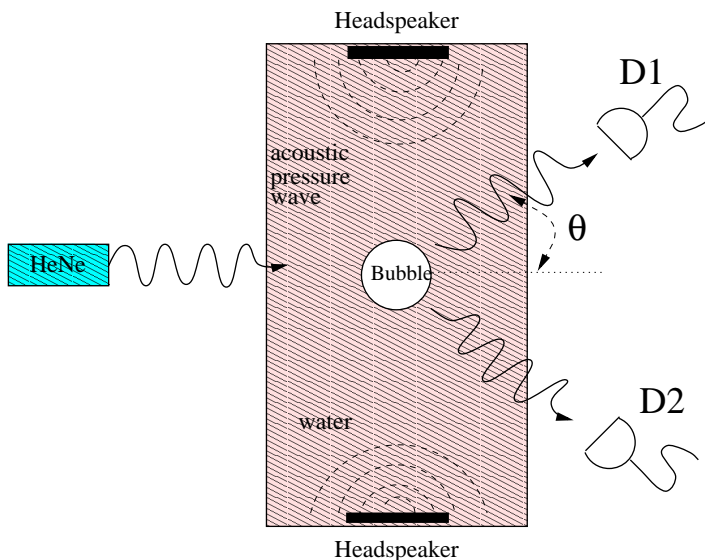


Fig. 1. Sketch of an experimental arrangement for light scattering measurements by a single sonoluminescent bubble. Basically, two types of measurements can be put forward: (i) The light elastically scattered by the bubble, illuminated by an external source (HeNe laser), is collected by the detector D1 as a function of time; (ii) The light flash emitted by the bubble (i.e., no external illumination is used) is collected by two detectors D1 and D2. This two signals can be subsequently correlated as a function of the angle between D1 and D2.

light is produced by a single, very bright air bubble, held in water under the action of ultrasound at intensity about 110 decibels (see Fig. 1). Experiments in heavy water with the bubble filled by a hydrogen isotope (either H2 and D2) have also been performed¹. Another interesting experimental fact is the sonoluminescence flash intensity dependence on the reactivity nature of the gases contained inside the bubble [5,6]. In particular, it has been shown that increasing the noble gas content (Xe, Ar, He) of a bubble stabilizes the bubble motion and increases its light emission intensity by an order of magnitude with respect the intensity emitted by the non-doped bubble.

As the pressure in the acoustic wave drops, the bubble, initially with a radius of a few microns, starts to inflate up to a radius of about 50 μm within a time interval of approximately 20 microseconds. Then, as the wave acoustic

¹ An extensive overview on the different aspects and new advances in single bubble sonoluminescence is out of the scope of this work. The interested reader can consult the WEB-page maintained by Dr. A. Levinson at the internet address <http://ne43.ne.uiuc.edu/ans/sonolum.html>. This WEB-page contains useful and interesting links to introductory-level papers on sonoluminescence. A more specialized-level review on the experimental state of the art up to date can be found in [4].

pressure starts to increase, the bubble drastically shrinks to $0.5\ \mu\text{m}$ in about 5 microseconds. Subsequently, its radius oscillates up and down by a few microns until it reaches the initial value. A new sound wave period hitting the bubble triggers the same process once again. Light emission occurs as the bubble compresses.

These variations of the bubble size have been analyzed by means of light scattering experiments [7]. In these experiments, laser light is scattered by the bubble surface and its angular distribution is detected (see Fig. 1). Large scattering angles (about 60°) are usually addressed. The intensity lobes are smoothed out. Then, a geometrical optics limit, according to which the measured intensity is proportional to the sphere surface, is employed to fit the bubble radius to the measured light intensity. However since the WKB approximation cannot be very accurate in this regime of bubble sizes, it has been recognized in these works that the uncertainty of radius determination by this method can be up to 20 percent for sizes of about $1\ \mu\text{m}$. Thus, other methods for determining the size, as well as the shape of the bubble, have been sought. The last advancement in this respect has been the determination of the angular correlations of the intensity of the emitted light, which we shall address in the next section.

The time of light emission during the sonoluminescent process is over 50 ps [8–10]. In this interval, assuming a speed of the bubble boundary of 1000 m/s, its radius changes by 50 nm, and the light is emitted from a small region within the pulsating bubble; then this light scatters from the bubble surface, subsequently being detected. Due to this small variation of the radius compared with its size, about $1\ \mu\text{m}$, the angular distribution of recorded intensity yields information of a frozen size and geometry [10,11] during the emission time.

The underlying cause of emission is however not clear at all yet. There are models that claim the existence of a shock wave due to the rapid movement of the bubble on compression, this giving rise to temperatures and pressures millions of times the normal ones, thus the air inside the cavity becoming plasma [7,12]. If this were true, this would suggest the existence of a fusion process. However, no released He atoms nor neutrons have been detected so far. Another theory proposes the existence of liquid jets due to the bubble oscillations [13–15]. This would induce electric currents which would radiate light. Also, there exist theoretical models that predict light emission from the liquid enclosing the bubble, due to the electric currents generate at the water breakdown [16]. Even the Casimir effect has been proposed as a possible mechanism for this phenomenon [17–19].

The flash spectrum is very similar to a blackbody one, and, with temperatures inside the bubble of the order of $10^6\ \text{K}$, (and pressures reaching 10^7 times the atmospheric one), this spectrum peaks within the 200 nm - 300 nm interval, thus likely being in the ultraviolet region. The peak power is about 30 mW. Since however, light at this frequency does not propagate in

water, this peak is very difficult to measure. As a single flash of the bubble does not contain enough light for data analysis, the authors of [11] measured angular correlations from many sonoluminescent shots at either the whole emission spectrum, or at *red*, ($\lambda > 500$ nm), or *blue*, ($260 \text{ nm} < \lambda < 380 \text{ nm}$) wavelengths. In this review it is seen that those experimental data provide a great deal of information, as a matter of fact the only one so far, in order to determine the size and shape of the pulsating bubble during the emission process.

1.2 Integral Equations for Light Scattering from Arbitrary Bodies

Let us consider an electromagnetic field, with electric and magnetic vectors $\mathbf{E}^{(i)}(\mathbf{r})$ and $\mathbf{H}^{(i)}(\mathbf{r})$, respectively, incident on a medium of permittivity ϵ occupying a volume V , constituted by multiple scattering volumes, namely, V is composed of parts V_1, V_2, \dots, V_N , each of which is limited by a surface S_1, S_2, \dots, S_N , respectively, (see Fig. 2). We shall denote by $\mathbf{r}^<$ the position vector of a generic point inside the volume V_i , and by $\mathbf{r}^>$ that of a generic point in the volume \hat{V} , which is outside all volumes V_i . The electric and magnetic vectors of a monochromatic field, satisfy, respectively, the wave equations [20]:

$$\nabla \times \nabla \times \mathbf{E}(\mathbf{r}) - k^2 \mathbf{E}(\mathbf{r}) = \mathbf{F}_e(\mathbf{r}), \quad (1)$$

$$\nabla \times \nabla \times \mathbf{H}(\mathbf{r}) - k^2 \mathbf{H}(\mathbf{r}) = \mathbf{F}_m(\mathbf{r}), \quad (2)$$

where k is the wavenumber, and \mathbf{F}_e and \mathbf{F}_m are the source terms that characterize the generation of electromagnetic waves. These terms are zero in the volume \hat{V} outside the medium; and inside are:

$$\mathbf{F}_e(\mathbf{r}) = 4\pi \left[\frac{ik}{c} \mathbf{j}(\mathbf{r}) + k^2 \mathbf{P}(\mathbf{r}) + ik \nabla \times \mathbf{M}(\mathbf{r}) \right], \quad (3)$$

$$\mathbf{F}_m(\mathbf{r}) = 4\pi \left[\frac{1}{c} \nabla \times \mathbf{j}(\mathbf{r}) - ik \nabla \times \mathbf{P}(\mathbf{r}) + k^2 \mathbf{M}(\mathbf{r}) \right], \quad (4)$$

In (3) and (4) \mathbf{P} and \mathbf{M} are the polarization and magnetization vectors, respectively; and \mathbf{j} represents the electric current density.

Let $\mathcal{G}(\mathbf{r}, \mathbf{r}')$ represent the dyadic Green function:

$$\mathcal{G}(\mathbf{r}, \mathbf{r}') = (\mathcal{I} + \frac{1}{k^2} \nabla \nabla) G(\mathbf{r}, \mathbf{r}'). \quad (5)$$

$G(\mathbf{r}, \mathbf{r}')$ being the outgoing spherical wave: $\exp(ik|\mathbf{r} - \mathbf{r}'|)/|\mathbf{r} - \mathbf{r}'|$. $\mathcal{G}(\mathbf{r}, \mathbf{r}')$ satisfies the equation:

$$\nabla \times \nabla \times \mathcal{G}(\mathbf{r}, \mathbf{r}') - k^2 \mathcal{G}(\mathbf{r}, \mathbf{r}') = 4\pi \delta(\mathbf{r} - \mathbf{r}') \mathcal{I}. \quad (6)$$

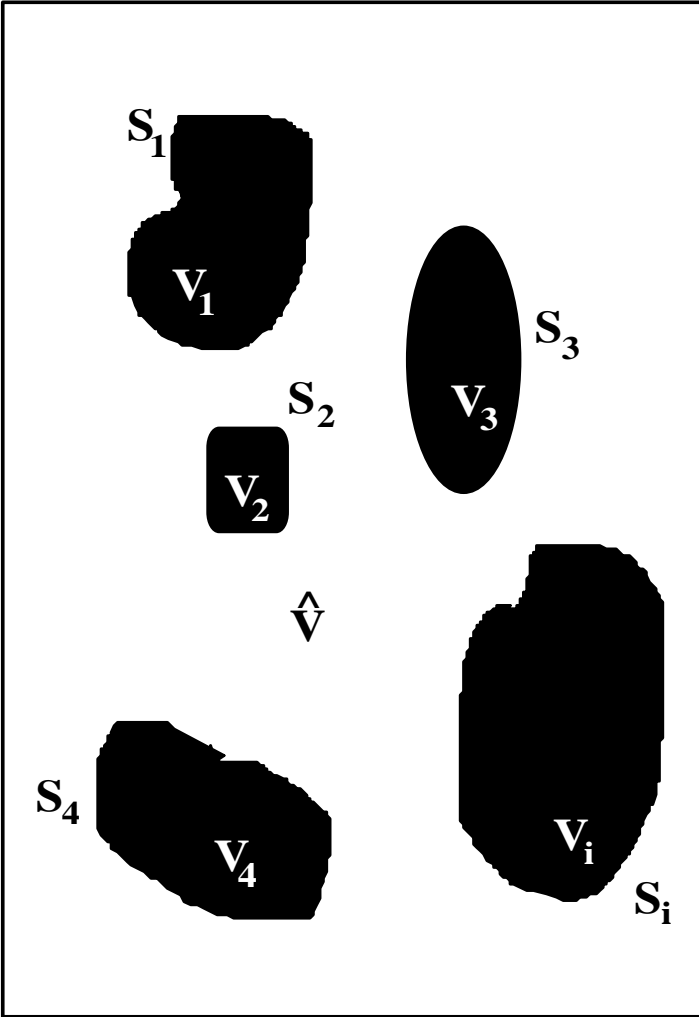


Fig. 2. Illustration for the scattering geometry.

For \mathbf{P} and \mathbf{Q} well behaved in a volume V surrounded by a surface S the vector form of Green's theorem reads [21]:

$$\int_V (\mathbf{Q} \cdot \nabla \times \nabla \times \mathbf{P} - \mathbf{P} \cdot \nabla \times \nabla \times \mathbf{Q}) dv = \int_S (\mathbf{P} \times \nabla \times \mathbf{Q} - \mathbf{Q} \times \nabla \times \mathbf{P}) \cdot \mathbf{n} ds, \quad (7)$$

\mathbf{n} being the unit outward normal.

Let us now apply (7) to the vectors: $\mathbf{P} = \mathcal{G}(\mathbf{r}, \mathbf{r}')\mathbf{C}$, (\mathbf{C} being a constant vector), and $\mathbf{Q} = \mathbf{E}(\mathbf{r})$. (The singularity of $\mathcal{G}(\mathbf{r}, \mathbf{r}')$ at the origin is integrable

for s -waves, whereas it is not for p -waves, (cf. e.g. [20] and [22]). Taking (1) and (6) into account, we obtain:

$$\int_V \mathbf{E}(\mathbf{r}') \delta(\mathbf{r} - \mathbf{r}') dv = \frac{1}{4\pi} \int_V \mathbf{F}_e(\mathbf{r}') \cdot \mathcal{G}(\mathbf{r}, \mathbf{r}') dv - \frac{1}{4\pi} \mathbf{S}_e(\mathbf{r}). \quad (8)$$

where \mathbf{S}_e is:

$$\mathbf{S}_e(\mathbf{r}) = \nabla \times \nabla \times \int_S (\mathbf{E}(\mathbf{r}') \frac{\partial G(\mathbf{r}, \mathbf{r}')}{\partial \mathbf{n}} - G(\mathbf{r}, \mathbf{r}') \frac{\partial \mathbf{E}(\mathbf{r}')}{\partial \mathbf{n}}) ds. \quad (9)$$

Equation (8) adopts different forms depending on where the points \mathbf{r} and \mathbf{r}' are considered. The wavenumber k entering in (8) is: $k = k_0 \sqrt{\epsilon}$ or $k = k_0$ according to whether \mathbf{r}' is in V or in \hat{V} , respectively, $k_0 = 2\pi/\lambda$. By means of straightforward calculations one obtains:

a) If \mathbf{r} and \mathbf{r}' belong to any of the volumes V_i , ($i = 1, 2, \dots, N$), namely, V becomes either of the volumes V_i :

$$\mathbf{E}(\mathbf{r}^<) = \frac{1}{4\pi} \int_{V_i} \mathbf{F}_e(\mathbf{r}') \cdot \mathcal{G}(\mathbf{r}^<, \mathbf{r}') dv - \frac{1}{4\pi} \mathbf{S}_i^{(in)}(\mathbf{r}^<). \quad (10)$$

where:

$$\mathbf{S}_i^{(in)}(\mathbf{r}^<) = \nabla \times \nabla \times \int_{S_i} (\mathbf{E}_{in}(\mathbf{r}') \frac{\partial G(\mathbf{r}^<, \mathbf{r}')}{\partial \mathbf{n}} - G(\mathbf{r}^<, \mathbf{r}') \frac{\partial \mathbf{E}_{in}(\mathbf{r}')}{\partial \mathbf{n}}) ds. \quad (11)$$

In (11) \mathbf{E}_{in} represents the limiting value of the electric vector on the surface S_i taken from inside the volume V_i . Equation (10) shows that the field inside each of the scattering volumes V_i does not depend on the sources generated in the other volumes.

b) If \mathbf{r} belongs to any of the volumes V_i , namely, V becomes V_i , and \mathbf{r}' belong to \hat{V} :

$$0 = \mathbf{S}_{ext}(\mathbf{r}^<). \quad (12)$$

In (12) \mathbf{S}_{ext} is:

$$\mathbf{S}_{ext}(\mathbf{r}^<) = \sum_i \mathbf{S}_i^{(out)}(\mathbf{r}^<) - \mathbf{S}_\infty(\mathbf{r}^<), \quad (13)$$

where:

$$\mathbf{S}_i^{(out)}(\mathbf{r}^<) = \nabla \times \nabla \times \int_{S_i} (\mathbf{E}(\mathbf{r}') \frac{\partial G(\mathbf{r}^<, \mathbf{r}')}{\partial \mathbf{n}} - G(\mathbf{r}^<, \mathbf{r}') \frac{\partial \mathbf{E}(\mathbf{r}')}{\partial \mathbf{n}}) ds. \quad (14)$$

In (14) the surface values of the electric vector are taken from the volume \hat{V} outside the volumes V_i . The normal \mathbf{n} now points towards inside each of the volumes V_i .

Also, \mathbf{S}_∞ has the same meaning as (14), but with the surface of integration now being a large sphere whose radius will eventually tend to infinity. It is not difficult to see that $-\mathbf{S}_\infty$ in (13) is equal to 4π times the incident field $\mathbf{E}^{(i)}(\mathbf{r}^<)$ (cf. [20] and [23]). Therefore (13) becomes finally:

$$0 = \mathbf{E}^{(i)}(\mathbf{r}^<) + \frac{1}{4\pi} \sum_i \mathbf{S}_i^{(out)}(\mathbf{r}^<). \quad (15)$$

Equation (15) is the *extinction theorem* for the electromagnetic field in a system composed of an arbitrary number of scattering bodies, each of which is limited by the surface S_i . Note that when this equation is used as a non-local boundary condition, the unknown *sources* to be determined, given by the limiting values of $\mathbf{E}(\mathbf{r}')$ and $\partial\mathbf{E}(\mathbf{r}')/\partial\mathbf{n}$ on each of the surfaces S_i , (cf. Eq.(14)), appear coupled to those corresponding sources on all the other surfaces S_j , $j \neq i$.

Following similar arguments, one obtains:

c) For \mathbf{r} belonging to \hat{V} and \mathbf{r}' belonging to any of the volumes V_i , namely, V becoming V_i :

$$0 = \frac{1}{4\pi} \int_{V_i} \mathbf{F}_e(\mathbf{r}') \cdot \mathcal{G}(\mathbf{r}^>, \mathbf{r}') dv - \frac{1}{4\pi} \mathbf{S}_i^{(in)}(\mathbf{r}^>), \quad (16)$$

with $\mathbf{S}_i^{(in)}$ given by Eq.(11), this time evaluated in $\mathbf{r}^>$.

d) For both \mathbf{r} and \mathbf{r}' belonging to \hat{V} :

$$\mathbf{E}(\mathbf{r}^>) = \mathbf{E}^{(i)}(\mathbf{r}^>) + \frac{1}{4\pi} \sum_i \mathbf{S}_i^{(out)}(\mathbf{r}^>), \quad (17)$$

Hence, the exterior field is the sum of the fields emitted from each scattering surface S_i with sources resulting from the coupling involved in the ET (15). The other important case corresponds to a penetrable, optically homogeneous, isotropic, non-magnetic and spatially nondispersive medium, (this applies to a real metal or a pure dielectric). In this case, (10) and (15) become, respectively:

$$\begin{aligned} \mathbf{E}(\mathbf{r}^<) &= -\frac{1}{4\pi k_0^2 \epsilon} \nabla \times \nabla \times \\ &\int_{S_i} (\mathbf{E}_{in}(\mathbf{r}') \frac{\partial G^{(in)}(\mathbf{r}^<, \mathbf{r}')}{\partial \mathbf{n}} - G^{(in)}(\mathbf{r}^<, \mathbf{r}') \frac{\partial \mathbf{E}_{in}(\mathbf{r}')}{\partial \mathbf{n}}) ds, \end{aligned} \quad (18)$$

$$\begin{aligned} 0 &= \mathbf{E}^{(i)}(\mathbf{r}^<) + \frac{1}{4\pi k_0^2} \nabla \times \nabla \times \\ &\sum_i \int_{S_i} (\mathbf{E}(\mathbf{r}') \frac{\partial G(\mathbf{r}^<, \mathbf{r}')}{\partial \mathbf{n}} - G(\mathbf{r}^<, \mathbf{r}') \frac{\partial \mathbf{E}(\mathbf{r}')}{\partial \mathbf{n}}) ds. \end{aligned} \quad (19)$$

whereas (16) and (17) yield:

$$0 = \frac{1}{4\pi k_0^2} \nabla \times \nabla \times \int_{S_i} (\mathbf{E}_{in}(\mathbf{r}') \frac{\partial G^{(in)}(\mathbf{r}^>, \mathbf{r}')}{\partial \mathbf{n}} - G^{(in)}(\mathbf{r}^>, \mathbf{r}') \frac{\partial \mathbf{E}_{in}(\mathbf{r}')}{\partial \mathbf{n}}) ds, \quad (20)$$

$$\mathbf{E}(\mathbf{r}^>) = \mathbf{E}^{(i)}(\mathbf{r}^>) + \frac{1}{4\pi k_0^2 \epsilon} \nabla \times \nabla \times \sum_i \int_{S_i} (\mathbf{E}(\mathbf{r}') \frac{\partial G(\mathbf{r}^>, \mathbf{r}')}{\partial \mathbf{n}} - G(\mathbf{r}^>, \mathbf{r}') \frac{\partial \mathbf{E}(\mathbf{r}')}{\partial \mathbf{n}}) ds. \quad (21)$$

In (18) and (20) "in" means that the limiting values are taken on the surface from inside the volume V_i ; note that this implies for both $G^{(in)}$ and \mathbf{E}_{in} that $k = k_0 \sqrt{\epsilon}$.

The saltus conditions:

$$\mathbf{n} \times [\mathbf{E}_{in}(\mathbf{r}^<) - \mathbf{E}(\mathbf{r}^>)] = 0, \quad \mathbf{n} \times [\mathbf{H}_{in}(\mathbf{r}^<) - \mathbf{H}(\mathbf{r}^>)] = 0 \quad (22)$$

across the surface S_i permit to find both \mathbf{E} and $\partial \mathbf{E} / \partial \mathbf{n}$ from either the pair (20) and (21), or, equivalently, from the pair Eqs.(18) and (19), as both $\mathbf{r}^>$ and $\mathbf{r}^<$ tend to a point in S_i . Then the scattered field outside the medium is given by the second term of (21).

In the next section, we apply this theory to the light created at the center of a sonoluminescent bubble and scattered by its surface. In this case, the incident field $\mathbf{E}^{(i)}$ is a spherical wave which hits the bubble surface *from inside*. The non-local boundary condition to use are (20) and (21), slightly modified to account for the fact that now the scattering volumes V_i reduce just to one V : the bubble, whose surface we shall denote as S . It is within this volume V where the incident field exists. Therefore, Eqs. (20) and (21) become, respectively:

$$0 = \mathbf{E}^{(i)}(\mathbf{r}^<) + \frac{1}{4\pi k_0^2} \nabla \times \nabla \times \int_S (\mathbf{E}_{in}(\mathbf{r}') \frac{\partial G^{(in)}(\mathbf{r}^<, \mathbf{r}')}{\partial \mathbf{n}} - G^{(in)}(\mathbf{r}^<, \mathbf{r}') \frac{\partial \mathbf{E}_{in}(\mathbf{r}')}{\partial \mathbf{n}}) ds. \quad (23)$$

$$\mathbf{E}(\mathbf{r}^>) = -\frac{1}{4\pi k_0^2 \epsilon} \nabla \times \nabla \times \int_S (\mathbf{E}(\mathbf{r}') \frac{\partial G(\mathbf{r}^>, \mathbf{r}')}{\partial \mathbf{n}} - G(\mathbf{r}^>, \mathbf{r}') \frac{\partial \mathbf{E}(\mathbf{r}')}{\partial \mathbf{n}}) ds, \quad (24)$$

2 Distribution of Radiated Light and Angular Correlations

Figures 3(a)-3(d) depict the shape and size of four of the several bubble geometries that we have tried for the analysis, and that are in principle compatible with arguments previously reported. These four sections correspond to the cut of the bubble by the plane at which the angular distribution of emitted light is being calculated as a function of θ (i.e., the plane defined by the position of the two detectors and the center of the bubble). The light is radiated by the point source marked by a dot at the center of each of these air bubbles. On scattering of this light wave by the bubble surface, one has a scattered field in the surrounding water which is expressed as [20]:

$$\varphi_{(s,p)}^\lambda(\theta) = \frac{i}{4} \int_D d\mathbf{r}' \left[\sqrt{\epsilon} (\mathbf{n}' \cdot \mathbf{k}_\theta) \varphi_{(s,p)}^\lambda(\mathbf{r}') - i \frac{\partial \varphi_{(s,p)}^\lambda(\mathbf{r}')}{\partial \mathbf{n}'} \right] \exp(i\sqrt{\epsilon} \mathbf{k}_\theta \cdot \mathbf{r}'). \quad (25)$$

The integral in (25) is extended to the bubble surface D . ϵ is the permittivity of water, \mathbf{k}_θ is the wave vector along the observation direction defined by the angle θ , $\varphi_{(s,p)}^\lambda$ represents the boundary value at the bubble surface D of the light wavefield in the surrounding water at the λ -wavelength either for s (TE waves) or p (TM waves) polarization. \mathbf{n}' is the local outward surface normal.

The boundary values φ and $\partial\varphi/\partial\mathbf{n}'$ are found from the non-local boundary conditions (we omit the subindices and superindices) [20]:

$$\varphi(\mathbf{r}) = \frac{1}{4\pi} \int_D d\mathbf{r}' \left[\frac{\partial G(\mathbf{r}, \mathbf{r}')}{\partial \mathbf{n}'} \varphi(\mathbf{r}') - G(\mathbf{r}, \mathbf{r}') \frac{\partial \varphi(\mathbf{r}')}{\partial \mathbf{n}'} \right], \quad (26)$$

$$0 = \frac{ij_0 k \sqrt{\epsilon_B}}{c} G_2(\mathbf{r}, \mathbf{r}') - \frac{1}{4\pi} \int_D d\mathbf{r}' \left[\frac{\partial G_B(\mathbf{r}, \mathbf{r}')}{\partial \mathbf{n}'} \varphi_B(\mathbf{r}') - G_B(\mathbf{r}, \mathbf{r}') \frac{\partial \varphi_B(\mathbf{r}')}{\partial \mathbf{n}'} \right]. \quad (27)$$

$G(\mathbf{r}, \mathbf{r}')$ is the spherical wave Green's function: $\exp(ik\sqrt{\epsilon}R)/R$, $R = |\mathbf{r} - \mathbf{r}'|$, $k = 2\pi/\lambda$, ϵ_B is the permittivity of the air within the bubble, c is the speed of light in vacuum, $G_B = \exp(ik\sqrt{\epsilon_B}R)/R$, $R = |\mathbf{r} - \mathbf{r}'|$, φ_B denotes the limiting value at the bubble surface of the light field inside the bubble. φ , φ_B , $\partial\varphi/\partial\mathbf{n}'$ and $\partial\varphi_B/\partial\mathbf{n}'$ are determined from (26) and (27) and the saltus conditions:

$$\varphi = \varphi_B, \quad (28)$$

$$\alpha^{-1} \partial \varphi / \partial \mathbf{n}' = \alpha_B^{-1} \partial \varphi_B / \partial \mathbf{n}', \quad (29)$$

where α and α_B are both either equal to 1 for s -polarization, or to ϵ and ϵ_B for p -polarization, respectively.

The emitted intensity in the water in an interval of wavelengths $[\lambda_1, \lambda_N]$ then is:

$$I(\theta) = \sum_{\lambda=\lambda_1}^{\lambda=\lambda_N} P_\lambda I_\lambda(\theta) = \sum_{\lambda} P_\lambda \left[|\varphi_s^\lambda(\theta)|^2 + |\varphi_p^\lambda(\theta)|^2 \right], \quad (30)$$

where we have added the intensities over all wavelengths in the above mentioned interval with relative weights P_λ , given by the sonoluminescent spectral distribution, P_λ reported in [12]. Also, we have considered unpolarized light given by the incoherent superposition of the two states of polarization s and p in the plane of measurement.

It is worth to note that the incoherent superposition of scattered intensities given by (30) implies the creation of a total *effective* intensity $I(\theta)$, which is *partially coherent* [24]. Furthermore, the degree of coherence of $I(\theta)$ is inversely proportional to the sonoluminescent spectral distribution P_λ . Namely, the degree of coherence of $I(\theta)$ is narrower the broader P_λ is ².

The angular distribution of scattered intensity corresponding to each of the four shapes is shown in Figs. 3(a)-3(d) at the four different wavelengths indicated there. The dielectric permittivities ϵ and ϵ_B are 1.77 and 1, respectively. Even for the ellipsoidal bubble, notwithstanding its small eccentricity, an interference pattern, on account of the scattering from the bubble surface, appears. Note, however, that the contrast of these intensities increases with the irregularity of the surface.

The angular correlation function of intensities is calculated as:

$$C(\Delta\theta) = \frac{\langle \{I(\theta) - \langle I(\theta) \rangle\} \{I(\theta + \Delta\theta) - \langle I(\theta + \Delta\theta) \rangle\} \rangle}{\langle I(\theta) \rangle \langle I(\theta + \Delta\theta) \rangle}, \quad (31)$$

where $\langle \cdot \rangle$ denotes ensemble average over the different realizations corresponding to the random orientations of the bubble at different flashes, as reported by the experiments. On using the ergodic property of the random intensities, this average can actually be performed over the θ -argument as: $\langle \cdot \rangle = \int_0^{2\pi} (\cdot) d\theta$.

² This issue has important consequences. For instance, in several experimental situations, the width of the sonoluminescent temporal pulse is much larger than the fluctuation time of the bubble dynamics (i.e., large bubble gas concentrations and driving pressures). In this case, our theory immediately indicates that this has a net effect of diminishing the temporal coherence length of the detected light. In consequence, much weaker, or even negligible, angular correlations would be obtained. Hence, the track about the bubble morphology would be lost even in the case in which the bubble collapse is asymmetric.

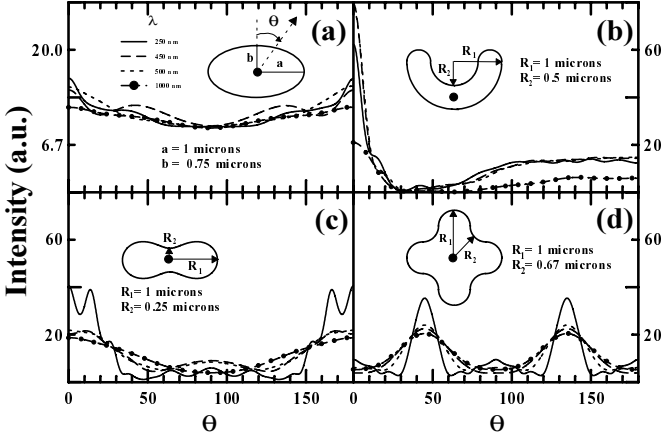


Fig. 3. Angular distribution of scattered intensity by an air bubble ($\epsilon_B = 1$) immersed in water ($\epsilon = 1.77$). The light source is assumed to be point-like at the bubble origin (marked in the insets as a point). Four different wavelengths are considered: $\lambda = 250$ nm (solid line), $\lambda = 450$ nm (long-dashed line), $\lambda = 500$ nm (short-dashed line), and $\lambda = 1000$ nm (short-dashed line with circles). 3(a): Ellipsoidal geometry. Size parameters: $a = 1 \mu\text{m}$, $b = 0.75 \mu\text{m}$. 3(b): 'Single-jet' geometry. Size parameters: $R_1 = 1 \mu\text{m}$, $R_2 = 0.5 \mu\text{m}$. 3(c): 'Double-jet' geometry. Size parameters: $R_1 = 1 \mu\text{m}$, $R_2 = 0.25 \mu\text{m}$. 3(d): 'Fourfold' geometry. Size parameters: $R_1 = 1 \mu\text{m}$, $R_2 = 0.67 \mu\text{m}$. The periodicity in the measured angular correlations [11] excludes the geometries of Figs. 3(b) and 3(d).

It is worth noticing that $I(\theta)$ and $C(\theta)$ have both the same angular periodicity, a fact that will be used below to select the bubble geometry.

From the intensity distributions of Figs. 3(a)-3(d) it is seen that only the intensity correlation functions of geometries with one axis of symmetry have a variation period between 0° and 180° , as established by the experiment of [11]. This pertains to the shapes of Figs. 3(a) and 3(c). The correlation function for the geometry of Fig. 3(b) has a period between 0° and 360° , and that for the shape of Fig. 3(d) has a fourthfold symmetry, thus its period is between 0° and 90° . Therefore, this fact rules out the validity of these last two geometries.

On the other hand, concerning the geometries of Figs. 3(a) and 3(c), (ellipse and oval, respectively), we present the angular correlation of the incoherent superposition of scattered intensities, which are distributed according to the calibrated spectral density of sonoluminescence reported in Ref. [11], for light scattered from the ellipsoid (Fig. 4(a)) and from the oval (Fig. 4(b)).

In order to get a realistic comparison with the experimental data, noise has been added to each of those signal intensities, such that $\sigma^2 / \langle I_\lambda \rangle^2 = 10^{-3}$, σ^2 being the noise variance and $\langle I_\lambda \rangle$ denoting the mean value of the

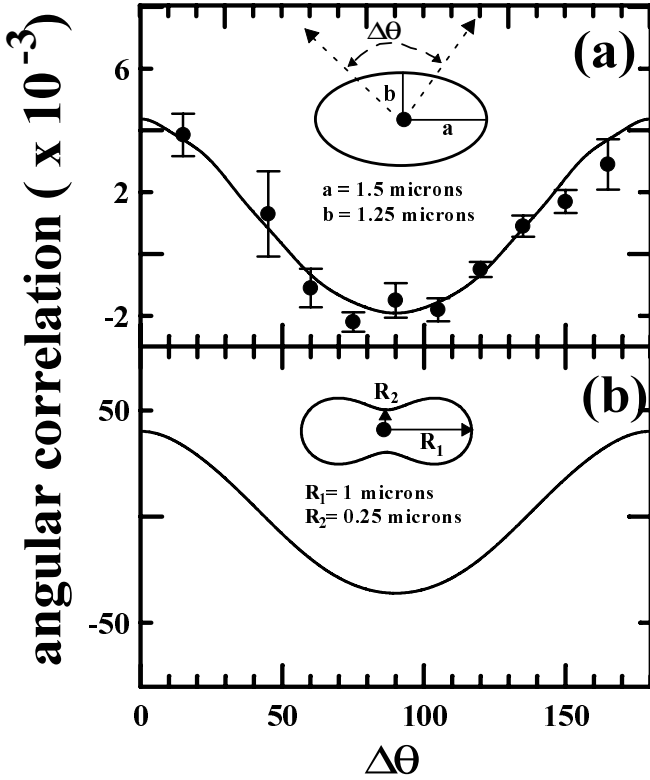


Fig. 4. Angular correlation of light intensity scattered by the bubble surface. The scattered intensity spectral distribution I^λ at fixed observation angle θ has been normalized to the full sonoluminescence flash spectrum (data taken from [12], Fig.1). 4(a): Ellipsoidal geometry. Size parameters: $a = 1.5 \mu\text{m}$, $b = 1.25 \mu\text{m}$. 4(b): Double jet geometry. Size parameters: $R_1 = 1 \mu\text{m}$, $R_2 = 0.25 \mu\text{m}$. The experimental data in Fig. 4(a) (circles) have been taken from [11], Fig. 1. The magnitude of the experimental angular correlation [11] rules out the geometry of Fig. 4(b).

scattered intensity at the λ -wavelength. Taking into account this fact, the new correlation function $C'(\Delta\theta)$ becomes now

$$C'(\Delta\theta) = C(\Delta\theta) + \sigma^2 / \langle I_\lambda \rangle^2, \quad (32)$$

where $C(\Delta\theta)$ is given in Eq. (31).

The addition of the noise term $\sigma^2 / \langle I(\theta) \rangle^2$ has important consequences: the interval of values of C' is not centered at $C' = 0$, but C' appears shifted towards positive values, also observed in the experimental values [11]. Figures 4(a), 5(a) and 5(b) reflect this fact.

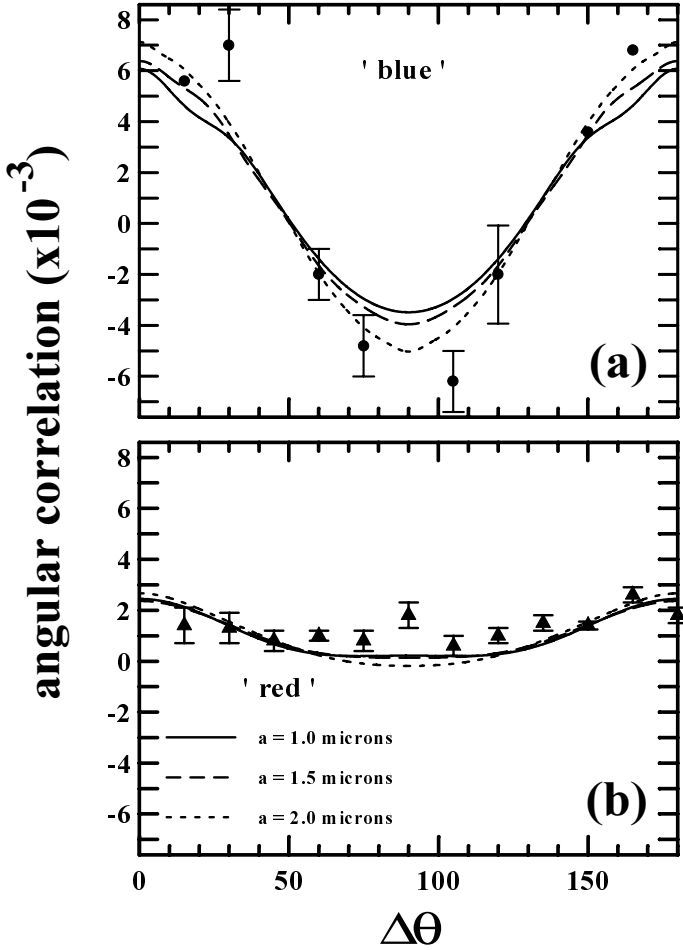


Fig. 5. Angular correlation of light intensity scattered by an ellipsoidal bubble with eccentricity $e = a/b - 1 = 0.2$. Three different sizes are considered: $a = 1\mu\text{m}$ (solid line), $a = 1.5\mu\text{m}$ (long-dashed line), and $a = 2\mu\text{m}$ (short-dashed line). The scattered intensity spectral distribution, taken from Fig.1 of [12], has been splitted both into the 'blue' sonoluminescence flash spectrum (Fig. 5(a), $280\text{ nm} < \lambda < 320\text{ nm}$), and the 'red' sonoluminescence flash spectrum (Fig. 5(b), $\lambda > 500\text{ nm}$). The experimental data (circles and triangles) are those from [11].

As seen, only the the angular correlation of light scattered from the ellipsoid varies in the range between -2 and 4 parts per thousand as reported in the experiments of [11]. The one corresponding to light emanating from the oval takes on a much a broader range of values, as it corresponds to scattered intensities with larger contrast than those from the ellipsoid (cf. Figs. 3(a) and 3(c)). Hence, we conclude that the oval shape should be also excluded, (incidentally, observe that the even larger contrast in Figs. 3(b) and 3(d) also rules out the geometries corresponding to these two figures).

Once we have concluded that only the ellipsoid geometry is compatible with the experiments, we proceed with the search for its size. Figures 5(a) and 5(b) show the angular correlation of scattered light for the incoherent superposition of intensities, following the sonoluminescent spectral distribution as before. However, now the addition of intensities is performed at two different intervals of wavelengths, namely, for wavelengths varying either larger than 500 nm for *red light*, or between 200 nm and 300 nm for *blue light*. The bubble is an ellipsoid with a being either $a = 1.0$ μm , 1.5 μm or 2 μm ; the eccentricity $e = a/b - 1$ being $e = 0.2$ in all cases. A one per thousand noise have been added to the scattered intensity data as before. From these two figures we observe an excellent agreement with the experimental data, within the estimated error in the measurements, although Fig. 5(a) indicates that the elliptic bubble with $a = 2$ μm matches the best for the blue light.

3 Conclusions

In this review we have given the theory of light scattering from the surface of a sonoluminescent bubble. This study permits to determine the shape and size of a sonoluminescent bubble on account of light correlation measurements at the emission instant. The conclusion is that the bubble surface is actually an ellipsoid of eccentricity very close to 0.2 and major radius between 1.5 μm and 2 μm . Calculations show that one tenth eccentricity deviations from 0.2 change by one order of magnitude the amplitude of the correlation function.

It should be remarked that this theory may be equally adapted to any experimental data that might appear in future. The conclusions on the bubble morphology would vary accordingly. For instance, if future experimental data show that the temporal width of the emitted sonoluminescent flash is much larger than the fluctuation time of the bubble hidrodynamic, our theory indicates that this fact has a net effect of shortening the temporal coherence length of the scattered light. Hence, much weaker, or even negligible, angular correlations would be obtained *whatever the bubble morphology is*.

Acknowledgments

Work supported by the Spanish DGICYT and the EU (Sprit and HCM programs).

References

1. Gaitan, D.F., Crum, L.A. (1990): Observation of sonoluminescence from a single, stable cavitation bubble in a water/glycerine mixture. *Frontiers of Non-linear Acoustics*. 12th ISNA. Elsevier Applied Science, London, 459-463
2. Barber, B.P., Putterman, S.J. (1991): Observations of synchronous picosecond sonoluminescent. *Nature* **352**, 318-320.
3. Gaitan, D.F., Felipe, D., Crum, L.A., Church, C.C. and Roy, R. A. (1992): Sonoluminescence and bubble dynamics for a single, stable, cavitation bubble. *J. Acoust. Soc. Am.* **91**, 3166-3183
4. Barber B.P., Hiller R.A., Lofstedt R., Putterman S. J., Weninger K. R. (1997): Defining the unknowns of sonoluminescence. *Phys. Rep.* **281**, 65-143
5. Hiller, R., Weninger, K., Putterman, S.J. and Barber, B. P. (1994): Effect of noble gas doping in single-bubble sonoluminescence. *Science* **266**, 248-250
6. Matula, T.J., Crum, L. A. (1998): Evidence for gas exchange in single-bubble sonoluminescence. *Phys. Rev. Lett.* **80**, 865-868
7. Barber, B.P. and Putterman, S.J. (1992): Light scattering measurements of the repetitive supersonic implosion of a sonoluminescing bubble. *Phys. Rev. Lett.* **69**, 3839-3842
8. Rigorously speaking, the time of light emission during the sonoluminescent process varies in the interval $[50, 250]ps$. Basically, this time of light emission depends on the range of gas concentration and driving pressure values used in the experiments. The interested reader can consult Refs. [9] and [10] for more details. Through our work, we shall assume that the sonoluminescent flash temporal width is equal or less than $50ps$ (i.e., low gas concentrations and driving pressures).
9. Gomp, B., Gunther, R., Nick, G., Pecha, R., and Eisenmengar, W. (1997): Resolving sonoluminescence pulse width with time-correlated single photon counting. *Phys. Rev. Lett.* **79**, 1405-1408
10. Hiller, R.A., Putterman, S.J., and Weninger, K.R. (1998): Time-resolved spectra of sonoluminescence. *Phys. Rev. Lett.* **80**, 1090-1093
11. Weninger, K., Putterman, S.J. and Barber, B.P. (1996): Angular correlations in sonoluminescence: Diagnostic for the sphericity of a collapsing bubble. *Phys. Rev. E* **54**, 2205-2208
12. Hiller, R., Putterman, S.J. and Barber, B.P. (1992): Spectrum of synchronous picosecond sonoluminescence. *Phys. Rev. Lett.* **69**, 1182-1184
13. Prosperetti, A. (1996): A new mechanism for sonoluminescence. *J. Acoust. Soc. Am.* **101**, 2003-2007
14. Longuet-Higgins, M.S. (1997): Particle drift near an oscillating bubble. *Proc. R. Soc. Lond. A* **453**, 1551-1568
15. Lepoint, T., DePauw, D., Lepoint-Mullie, F., Goldman, M., and Goldman, A. (1997): Sonoluminescence: an alternative 'electrodynamic' hypothesis. *J. Acoust. Soc. Am.* **101**, 2012-2030.
16. García, N., and Levanyuk, A. (1996): Sonoluminescence: a new electrical breakdown in water. *JETP Lett.* **64**, 909-913
17. Schwinger J. (1993): Casimir light: the source. *Proc. Natl. Acad. Sci. U.S.A.* **90**, 2105-2106
18. Eberlein, C., (1996): Sonoluminescence as quantum vacuum radiation. *Phys. Rev. Lett.* **76**, 3842-3845

19. García N., and Levanyuk A. (1997): Comment on 'Sonoluminescence as quantum vacuum radiation'. Phys. Rev. Lett. **78**, 2267
20. Nieto-Vesperinas, M., (1991): *Scattering and Diffraction in Physical Optics*, (Wiley, New York) Chap. 7.
21. Morse, M.P., and Feshbach, H., (1953): *Methods of Theoretical Physics*, (Mc Graw Hill, New York)
22. Nieto-Vesperinas, M., and Soto-Crespo, J.M., (1987): Monte Carlo simulations for the scattering of electromagnetic waves from perfectly conductive random rough surfaces. Opt. Lett. **12**, 979–981; Sanchez-Gil, J.A., and Nieto-Vesperinas, M. (1991): Light scattering from random rough dielectric surfaces. J. Opt. Soc. Am. A **8**, 1270–1286
23. Pattanayak, D.N., and Wolf, E. (1972): General form and a new interpretation of the Ewald-Oseen extinction theorem. Opt. Comm. **6**, 217–220
24. Mandel, L., and Wolf, E., (1995): *Optical Coherence and Quantum Optics*, (Cambridge University Press, New York) Ch. 4.